Journal of Alloys and Compounds 520 (2012) 105–113

Contents lists available at SciVerse ScienceDirect

Journal of Alloys and Compounds

journal homepage: www.elsevier.com/locate/jallcom

Mechanical consolidation of rapidly solidified Meso 20 alloy flakes – Structure and mechanical properties

L. Blaz[a,*], M. Sugamata[b], A. Kula[a], G. Wloch[a], J. Sobota[a]

[a] AGH-University of Science and Technology, Dept. Structure and Mechanics of Solids, Cracow, Poland
[b] Nihon University, College of Industrial Technology, Tokyo, Chiba, Japan

ARTICLE INFO

Article history:
Received 27 June 2011
Received in revised form
26 December 2011
Accepted 27 December 2011
Available online 9 January 2012

Keywords:
Rapid solidification
AA7000 series Aluminum alloy
Al–Mn alloy
Extrusion
TEM
EDS
SAD pattern analysis
Quasicrystals
μ-Al_6Mn phase
Dynamic precipitation

ABSTRACT

The mechanical properties and microstructure evolution of the rapidly solidified (RS) Meso 20 aluminum alloy, followed by mechanical consolidation of RS-flakes were investigated. Specimens of as-extruded material and the specimens solution treated at 773 K/30 min were tested in hot compression at temperatures ranging from 293 K to 773 K. It was found that the flow stress was reduced monotonically with deformation temperature within the used deformation temperature range. Expected dynamic precipitation hardening at the intermediate deformation temperatures for solution treated specimens was negligible. Concurrently, the crystallographic structure and the distribution of the particles did not correspond to the commonly known morphology of the highly disperse η', η precipitates and Al_6Mn particles that are usually reported for the industrial AA7000 series alloys. Due to the low-temperature extrusion method, most of the fine Mn-rich particles retained their quasicrystalline structure formed during the rapid solidification and following consolidation of the RS-flakes. The solution treatment of the as-extruded specimens at 773 K/30 min was found to result in the development of μ-Al_4Mn rod-like particles. The twinned structure of the particles points to their growth along $\langle 3\,\bar{3}\,0\,1\rangle$ direction.

1. Introduction

Common industrial methods for strengthening of aluminum alloys include careful selection of chemical composition, grain size refining methods, and heat treatment such as aging and precipitation hardening. Powder metallurgy (PM) and mechanical alloying (MA) of Al-based composites are less common methods for manufacturing high strength material, primarily because of the relatively high production cost [1–3]. Contrary to the MA method, rapid solidification (RS) is of a relatively low-cost and is often successfully used for production of fine grained materials. The most critical problem for the production of both the nano-structured RS alloys and the MA metallic composites is connected with the searching for a proper material composition and the processing methods to receive high stability of the structural components and the related mechanical properties at high temperatures.

Mechanical consolidation of the RS powders typically involves several steps such as pressing, vacuum degassing, followed then by hot extrusion of as-compressed metallic charge. The last step requires heating of the metallic charge, and is followed by high-temperature processing that results in the grain coarsening and ultimately reduction of high strength capability.

Rapid solidification method allows for grain refining, increase of the range of solid solubility, reduction of the alloying elements segregation, and evolution of advantageous morphology of both the intermediate phases and the equilibrium constituents. For example, the zinc content in conventionally cast AA7000 series aluminum alloys is limited to about 8% due to the inherent casting problem such as solute segregation and cracking.

On the other hand, rapid solidification enables reduction of zinc segregation and results in relatively homogeneous distribution of constituent phases. Moreover, alloys processed by RS may have increased zinc content. In consequence, the increased zinc content and the related precipitation hardening increases the strength of material [4,5]. In another example, addition of manganese in the cast AA7000 series is often utilized to limit the grain coarsening. However, the RS method, applied for manufacturing some of Al–Mn RS alloys, allows for oversaturation of manganese in the aluminum solid solution therefore enhancing the precipitation of fine Al–Mn

* Corresponding author at: AGH-University of Science and Technology, Faculty of Non-ferrous Metals, Department of Structure & Mechanics of Solids, Al. Mickiewicza 30, 30-059 Kraków, Poland. Tel.: +48 12 6172648; fax: +48 12 6325615.
E-mail address: blaz@agh.edu.pl (L. Blaz).

0925-8388/$ – see front matter © 2012 Elsevier B.V. All rights reserved.
doi:10.1016/j.jallcom.2011.12.142

type particles and resulting in increased strength due to the particle hardening.

In the commercial (cast) AA7000 series products the alloy composition and manufacturing conditions determine the dominant phases and their morphology [4–13]. Zn, Mg and Cu partition to the hardening phases and typical precipitates formed under slow cooling condition are: orthorhombic *S*-phase Al_2CuMg, which is formed at between 573 K and 713 K with the maximum fraction forming at 683 K, and hexagonal η-phase $Mg(Zn_2,AlCu)$ that precipitates below ~713 K with the maximum fraction forming below 483 K [10]. Prolonged annealing can result in the development of *T*-phase $Al_{32}(Mg,Zn)_{49}$. Aging usually leads to evolution of Zn-rich metastable phases η' and η ($MgZn_2$) which are the most effective precipitation-hardening phases in the AA7000 class of materials [5]. Precipitation at the low aging temperatures (below 460 K) usually follows the commonly known sequence of phase transformations: supersaturated solid solution (*sss*) → Guinier–Preston (GP) zones (spherical) → η' metastable phase (plate-like) → η phase $MgZn_2$ or $Mg(Zn_2,Al,Cu)$ → *T*-phase reported as $Al_{32}(Mg,Zn)_{49}$ [5,10,11] or $(Al,Zn)_{49}Mg_{32}$ [4,5,7,9] or $Al_2Mg_3Zn_3$ [5]. The particles of the η' and η hexagonal phase ($MgZn_2$) are usually observed for AA7000 alloys containing relatively high Zn/Cu, Mg ratio.

Number of researchers investigated precipitation sequence in solution-treated and aged Al–Zn–Mg alloys containing the Zn/Mg ratio close to the stoichiometry of the $MgZn_2$ phase [13–17]. For alloy aged within the temperature range of 323–473 K they reported development of GP zones followed by nucleation of the disperse η'-transition phase, which ultimately transforms to η ($MgZn_2$). Spherical GP zones can also form for alloy aged below 323 K, and they are practically stable during the initial stage of aging [13,14,17]. On the other hand, the GP zones can be practically eliminated from the aging sequence at 423 K in common industrial technologies, as they immediately transform to η' and η-particles [13]. Prolonged aging above 463 K results in the development of the ternary cubic *T*-phase formed from the pre-existing η-precipitates. Lattice parameters of $a = 0.497$ nm and $c = 0.554$ nm were reported for the metastable η' – hexagonal particles. However, a detailed analysis of the η'-particles revealed several types of particles varied in shape and particle/matrix crystallographic relation [4,13,15].

Rapid solidification of Al–14 at.%Mn alloy by means of the spinning method yields in evolution of intermetallics that exhibit quasicrystalline structure, as reported by Shetchman et al. [18]. Since that pioneer work number of experiments have been performed on aluminum–manganese materials (enriched with Fe, Cr, Mn, Pd, V, Co, Ni, Mo, Pt) to investigate rapid solidification effect on the development of quasicrystals. It was reported that the quasicrystalline structures often form with the departure from the equilibrium constitution [18,22–25,29]. Specifically, two metastable compounds with quasiperiodic structure either I – icosahedral or D – decagonal can be formed in the Mn-enriched aluminum alloys rapidly quenched from the melt (~10^6 K/s). Such metastable structure of quasicrystals transforms into Al_6Mn + (Al) during annealing at 670–773 K [26–29]. Similar nanoquasicrystalline structures are also formed during annealing above 573 K in electrodeposited Al–Mn alloys containing 12.3–15.8 at.% Mn [26,29]. Very high cooling rate used in the RS procedures for the manufacture of commercial AA7000 alloys, as well as electrodeposition of Al–Mn alloys, allows increasing the solubility of manganese even up to ~12% Mn. For example, manganese primary phase was not found in Al–4.4% Zn–2.7% Mg–0.2% Zr–(0.4–2.5%)Mn alloy rapidly solidified at the cooling rate of 10^3–10^4 K/s [30].

The basic challenge for the RS/PM technologies is related to the prevention of the structural component coarsening during the hot pressing and following the hot processing of the RS material. Therefore, the mechanical consolidation of RS powders should be performed at as low temperature as possible. Thus, instead of the commonly used hot extrusion methods, an advanced so-called KOBO extrusion can be recommended for the RS/PM material processing [31–33]. The method offers the advantage of omitting the charge preheating prior the extrusion. Even if a heating pulse occurs due to the intense deformation at a high extrusion ratio, its duration is likely to be short enough to avoid the noticeable coarsening of the fine RS structure. Furthermore, it is commonly known that the microstructure defects, flaws and porosity deteriorate the mechanical properties of PM materials [34,35]. In the consequence of the intense processing at a high extrusion ratio, which is available with the KOBO extrusion method, an effective homogenization of the processed PM material can be expected. Therefore, the advanced KOBO extrusion can be recommended for the RS/PM material processing, instead of the commonly used hot extrusion methods.

Experiments on the RS Meso 20 aluminum alloy (AA7000 series), described below, were performed in order to test the effect of rapid solidification and the powder consolidation procedures on the structure and mechanical properties of the material. Attention was paid to the material structure evolution during the annealing and the hot deformation of the material.

2. Material and experimental

Experiments were performed on the rapidly solidified (RS) Meso 20 alloy. Chemical composition of the alloy is shown in Table 1. The alloy was melted at ~1000 K and spray-deposited on a rotating water-cooled copper cylinder. Pressured argon gas was used for the melt atomization and protection of the powder's oxidation. The preliminary consolidation of the RS-flakes was performed utilizing vacuum compression at ~670 K and 100-tonn press. The as-compressed billets were then extruded utilizing KOBO extrusion method at cross-section reduction ratio of $\lambda = 19$ and extrusion rate of 30–60 cm/min. The method allowed for obtaining 7 mm diameter rods, without heating up of the charge that is used in the conventional processing route.

Specimens with dimensions 10 mm in length and 6 mm in diameter were machined from the as-extruded rod and used for investigating mechanical properties. Two sets of specimens were utilized: in as-extruded condition, and solution treated at 770 K for 30 min (ST) followed by water quenching. Compression tests at the constant true strain rate of 5×10^{-3} s^{-1} were performed at 293–773 K. The hot deformed samples were quenched in water for 3 s after the test completion. Flaked graphite was used to reduce the friction between the sample and the anvils.

Compressed specimens were sectioned parallel to the compression axis and used for structural evaluations and hardness test. Micro-hardness was measured on flat surface utilizing Vickers hardness tester and indenter load of 49 N. The average hardness value was calculated for 15–20 measurements.

Microstructural evaluations were performed by means of light and transmission electron microscopy (LM and TEM) techniques. JEM 2010 TEM equipped with scanning transmission electron microscopy (STEM) device and Oxford PENTAFET energy dispersive X-ray (EDX) analysis system was used. The EDX analysis system was controlled by means of the ISIS program, which facilitates both the single point analysis and the procedure for the multi-point EDX analysis, performed along the line marked in the previously taken STEM picture. The latter consists in making the EDX analyses at a predefined number of points uniformly distributed along the line marked in the STEM image. Element mapping and line-scan analyses were also available.

The computer-aided SAD pattern analyses were based on the LatticeCalc program, developed at AGH-UST. The program allows for a simple matching of the crystallographic data reported in literature with the interplanar distances and the corresponding angles measured from the SAD pattern.

Thin foils for the TEM/STEM observations were prepared using mechanical grinding followed by ion thinning in Gatan PIPS 691 unit.

Phase transformation study was conducted by means of differential scanning calorimetry (DSC) utilizing Tolledo TMA/SDTA 840 system. Tests were conducted at the temperature ranging from 293 K to 973 K. Samples were heated up at heating rate of 30 K/min.

Table 1
Chemical composition of Meso 20 alloy, in wt.%.

Zn	Mg	Cu	Fe	Si	Mn	Ag	Al
9.59	3.43	1.68	0.018	0.014	3.52	0.055	In balance

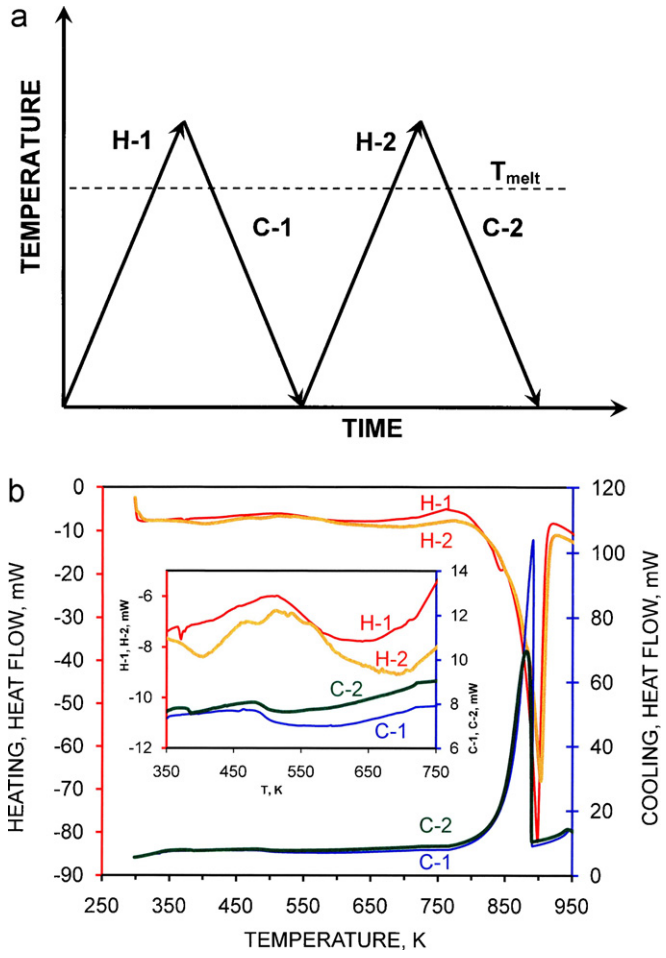

Fig. 1. DSC curves for the as-extruded material tested at heating/cooling rate 30 K/min: (a) scheme of consecutive heating/cooling cycles; (b) DSC results (inserted graph is displayed in expanded scale to show exothermic peaks at 450–550 K).

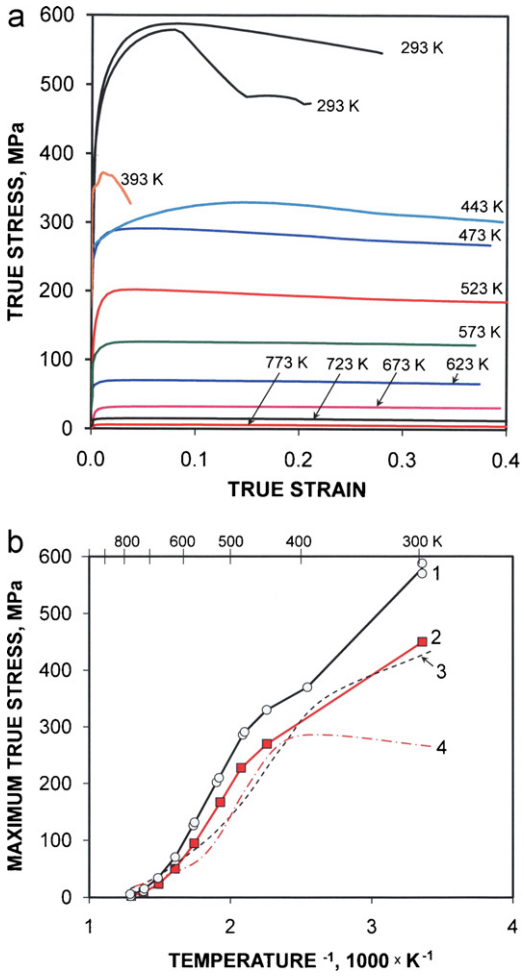

Fig. 2. Compression test results for RS Meso 20 alloy: (a) flow stress curves for as-extruded specimens (deformation temperature is marked in the figure); (b) effect of deformation temperature on the maximum flow stress, (1) as-extruded RS Meso 20 alloy, (2) RS Meso 20 specimens solution treated at 773 K/30 min and water quenched before testing, (3) as-extruded 7N01 (AA7005) industrial alloy, (4) 7N01 alloy solution treated at 743 K/1 h before testing [38].

3. Results and discussion

Consecutive DSC tests were performed at 293–950 K according to the scheme displayed in Fig. 1a. The obtained DSC curves are shown in Fig. 1b. The inset in Fig. 1b presents enlarged part of the DSC curves for better resolution of phase transformations. The exothermic peaks between temperatures 450 K and 550 K, observed during the first heating cycle (curve H-1 in Fig. 1b) correspond to the overlapped effect of recovery and precipitation sequences. The wide depression that occurs at 580–720 K results from the successive dissolution of the particles, which finally releases the grain boundaries and makes the recrystallization of the matrix possible at 750–800 K. After the re-melting of the sample during the first heating/cooling cycle, the material structure becomes relatively close to that of an industrial material, rather than that of the RS alloy. Therefore, the following heating/cooling DSC curves were found to present the typical exo- and endothermic peaks that are usually observed for the commercial AA7075 alloy. In particular, the separated peaks on the H-2 curve can be attributed to the precipitation of the metastable η' and η phases [36,37].

An enhanced endothermic effect observed at 810–900 K result from the melting of the material within temperature interval related to the solidus–liquidus range. Therefore, the following annealing and hot compression experiments were performed below 800 K in order to avoid the sample melting. The typical true stress–true strain curves for the as-extruded material are shown in Fig. 2a. The samples deformed at 293–393 K were fractured during the test as a result of the highly localized flow that begun after a few-percentage uniform strain. The variation of the strain from the sample fracture at a low deformation temperature may result from the accidentally occurring micro-defects (cracks or pores) at the as-extruded rods. At higher deformation temperature the fracture of the samples was not observed. The hot compression tests at 443–773 K were limited to $\varepsilon_t \cong 0.4$ to avoid the sample barreling at higher strains. The steady-state flow regime, observed at these temperatures, is typical for the aluminum alloys undergoing an intense dynamic recovery.

The second set of specimens (solution treated and quenched) was tested to investigate the expected effect of dynamic precipitation at intermediate deformation temperatures. The flow curves were similar in the shape and are not presented in Fig. 2a.

Maximum flow stress vs. inverse deformation temperature recorded for the both sets of specimens is shown in Fig. 2b. It may be noted in Fig. 2b that in spite of the flow stress reduction due to the annealing, the character of maximum flow stress change with temperature for the both sets is similar. One may conclude that the hardening effect from the dynamic precipitation is negligible. On the other hand, the exothermic effects on the DSC curves (Fig. 1) as well as the precipitation sequences reported in literature for the AA7000 series lead to the conclusion that the dynamic precipitation hardening might be expected for the solution treated samples

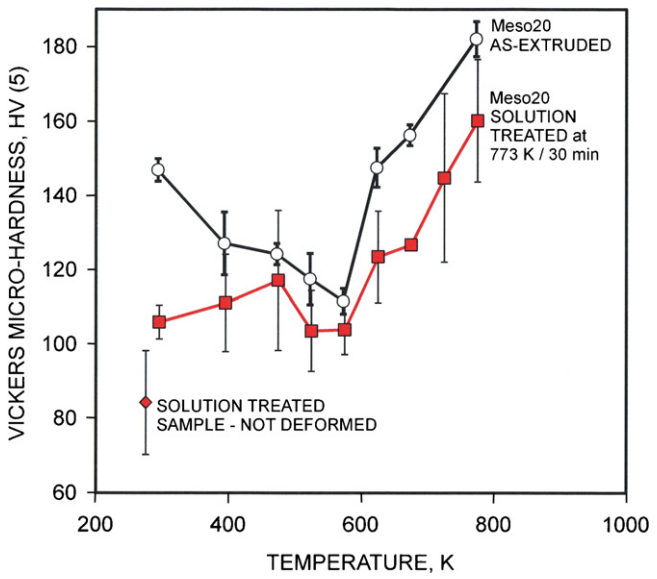

Fig. 3. Effect of deformation temperature on the hardness of as-extruded and solution treated RS Meso 20 alloy (773 K for 30 min) deformed $\varepsilon_t \cong 0.4$ by compression. The hardness of the solution treated and water quenched sample (not deformed) is marked for comparison.

deformed at 400–550 K [9–17]. For comparison, the curves for as-extruded and solution treated industrial 7N01 alloy (AA7005-series, composition in wt.%: Al–4.4% Zn, 1.4% Mg, 0.4% Mn, 0.6% Fe, 0.04% Si, 0.02% Cu) are presented in Fig. 2b [38]. Comparing curve 3 (as-extruded) with curve 4 (solution treated) it may be noted a remarkably difference manifested by slope change of curve 4 between 350 K and 450 K. This change is associated with the evident dynamic precipitation in the solution-treated 7N01 industrial alloy. The flow stress increase due to the dynamic precipitation is often observed for the solution treated materials and was reported for other precipitation-hardenable alloys [39–42].

The suppressed dynamic precipitation strengthening for the solution treated RS Meso 20 alloy can be related to the specific material structure. The fine grained structure and the refined Mn-rich particles in the RS material, which are relatively stable in hot deformation tests, result in the favoured heterogeneous precipitation of the η-type phase on the preexisting Mn-rich particles, grain boundaries, as well as other structural defects and inhomogeneities [5,11,44–46]. This seems to reduce the driving force for the homogeneous nucleation of very fine particles in the matrix, which is necessary for the effective hardening effect. Therefore, the "hump" on the flow stress vs. deformation temperature relation for the solution treated RS Meso 20 alloy is suppressed.

The effect of the deformation temperature on the material's hardness is shown in Fig. 3. The as-extruded material exhibited decrease in hardness with increasing deformation temperature up to 600 K, followed by the significant increase of hardness for deformation temperatures above 600 K. The observed hardness decrease can be attributed to the dynamic recovery, which is intensified with the increasing deformation temperature. However, the reason of the following hardness increase above ~600 K, is not clear. As the samples deformed close/above the solvus temperature had been quenched in water and stored at ~160 K until the hardness tests were performed, the effect of the natural aging should be very limited. Therefore, the hardening may likely be attributed to the solution hardening rather than the natural aging of the material.

The solution treated specimens exhibit slightly marked hardening at 400–500 K that result from the dynamic precipitation hardening [41,42]. However, due to the significant scatter of the hardness data, the dynamic precipitation effect cannot be explicitly confirmed.

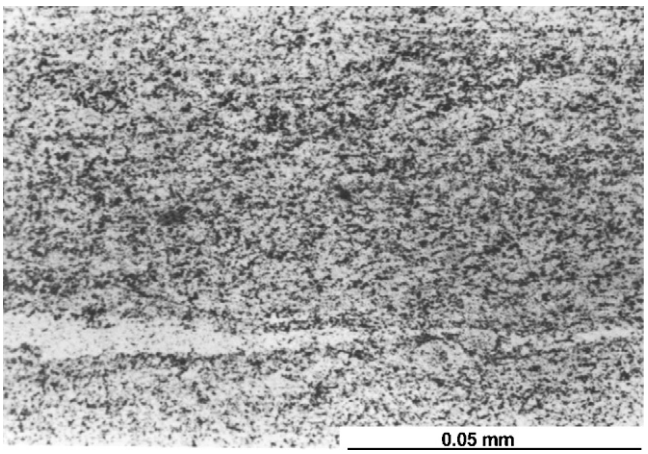

Fig. 4. Microstructure of RS Meso 20 as-extruded rod (light microscopy, longitudinal section).

3.1. Structural observations

In order to investigate the microstructural evolution, the LM and TEM structural observations were performed for the material at the each step of the processing route, specifically for the RS flakes, as-extruded and selected hot deformed specimens.

Typical microstructure of as-extruded material, observed at a low magnification (light microscopy, longitudinal section), is shown in Fig. 4. The highly refined particles were too small for a detailed analysis of their size with the use of the LM method. Some locally observed differences in the particles' morphology (see: brighten elongated area) correspond to the specific distribution of the particles in one of the preliminary RS flakes. The mentioned effect mostly depends on the spray drop size that affects the solidification rate of the particular RS flake and the resulted morphology of the particles. The porosity of the material, roughly estimated with the use of the statistical metallography method, was less than ~1%.

Typical STEM microstructure of as-solidified RS-flake is shown in Figs. 5 and 6. Fine, Mn-rich particles has formed during RS process. The average length and width of the particles, as measured from roughly 100 particles, is 11.5 nm and 8.6 nm, respectively.

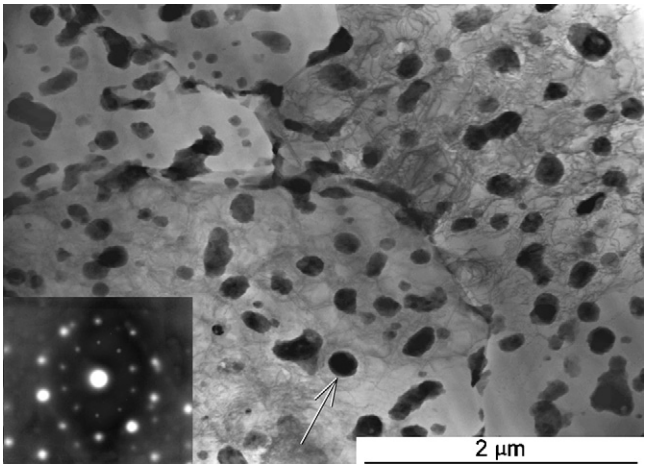

Fig. 5. STEM microstructure of the RS-flake. Inserted diffraction pattern was received from the particle marked in the picture. EDX spectrum from the particle is shown in Appendix A, Fig. A1.

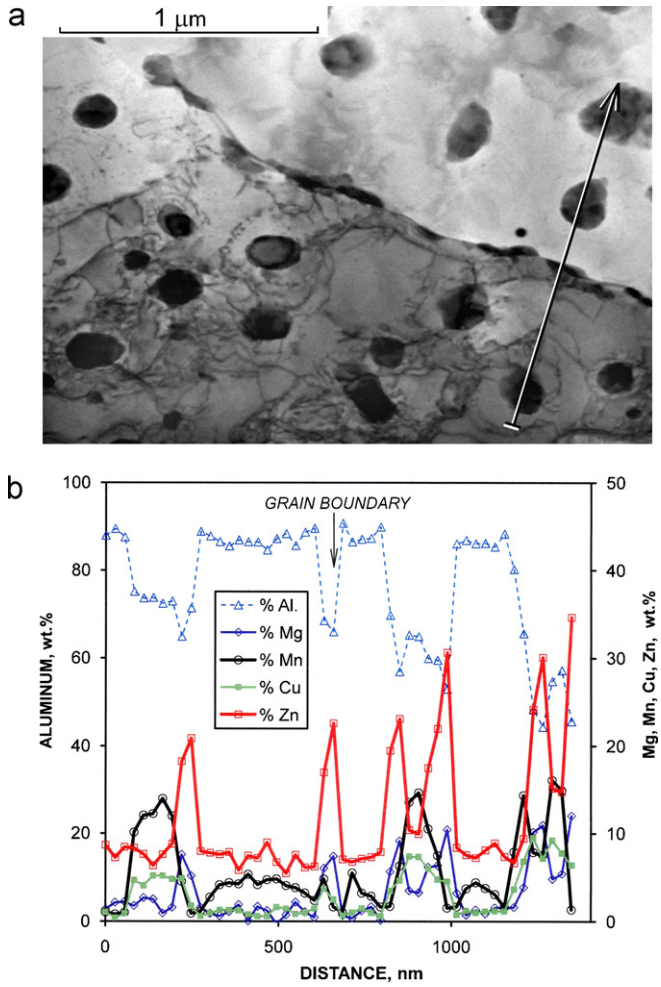

Fig. 6. Structure of Meso 20 RS-flake: (a) STEM image and (b) element distribution measured in EDX with the use of automatic stepping of the beam along the line marked in the STEM picture.

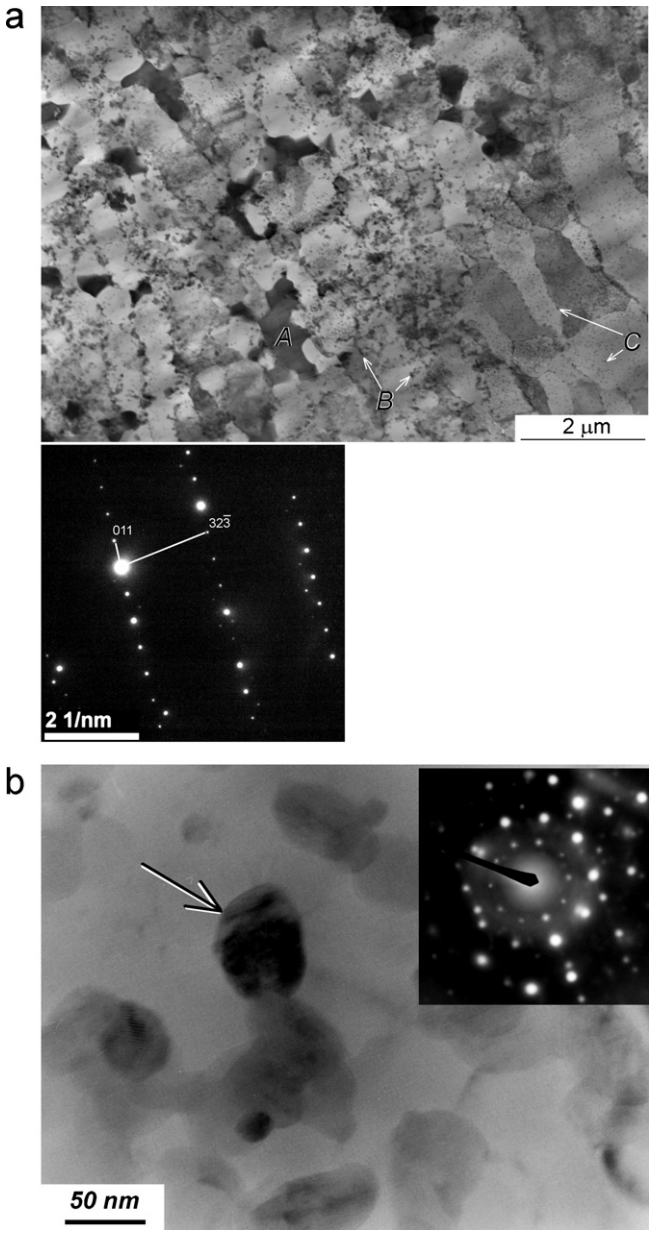

Fig. 7. Structure of the as-extruded rod: (a) STEM image and SAD pattern received from the coarse particle "A" and (b) Fine Mn-rich particle "B" observed at higher magnification by means of TEM (SAD pattern inserted). Fine (Zn, Mg)-rich particles are also marked "C" in STEM image.

The EDX analysis revealed a complex composition of the particles that were enriched in Al, Mn, Zn, Mg, Cu (typical EDX spectrum is shown in Appendix A, Fig. A1). The SAD pattern analysis performed for a few particles revealed a quasi-crystalline structure (see: SAD pattern inserted in Fig. 5). Similar quasicrystals of icosahedral symmetry were reported for rapidly solidified aluminum alloys containing Mn by Shetchman et al. [18] and others [19–26,29].

The EDX employing automatic stepping of the beam across the particles in STEM mode was performed to investigate distribution of elements in the structure. The example of STEM image and the corresponding elemental distribution along the line marked in the STEM image is presented in Fig. 6a and b, respectively. In Fig. 6a it may be seen that the particles precipitate as frequently at the grain boundaries as in the grain interiors. The elemental distribution, as in Fig. 6b, indicates that the both type of precipitates (at the grain interior and at the boundary) are rich in Zn, Cu and Mg. However, the interior of the three particles located at the matrix is rich in Mn. It may be clearly noted that Zn distribution line (and Mg line) is shifted relative to Mn one, and the peak sometimes is single, while the other times two peaks before and after the Mn peak are present. This result suggests that Zn-rich skin has heterogeneously grown as a second phase on the surface of the preliminary nucleated Mn-rich particles.

Typical STEM/TEM microstructure of the as-extruded material is presented in Fig. 7. Large, irregular in shape, A-type particles, 50–150 nm in size, were observed. The chemical composition of the A-type particles, identified in EDX, revealed the atomic ratio Al:Mg:Zn close to 2.2:2.7:3.1. It is very close to the stoichiometry reported for the $Al_2Mg_3Zn_3$ *T*-phase. The SAD pattern displayed in the figure confirmed the structure of the *T*-phase that was consistent with the similar observations reported by Chang et al. [30].

It has been found that the nano-sized B-particles (Mn-rich), shown in Fig. 7a, were still of decagonal symmetry, which was typical for most of the very fine quasicrystals observed in the RS flake. The quasicrystalline structure of the B-type particles was confirmed by the TEM and SAD pattern analysis (Fig. 7b). It is worth mentioning that similar experiments on the RS/PM Al–4.7Zn–2.5Mg–0.2Zr–2.5Mn (in wt.%) alloy were performed by Chang et al. [30]. They did not reveal any manganese primary phase precipitates in the RS powder. The following consolidation of the powders and the hot extrusion at 673 K were found to result in the development of orthorhombic Al_3Mn fine particles.

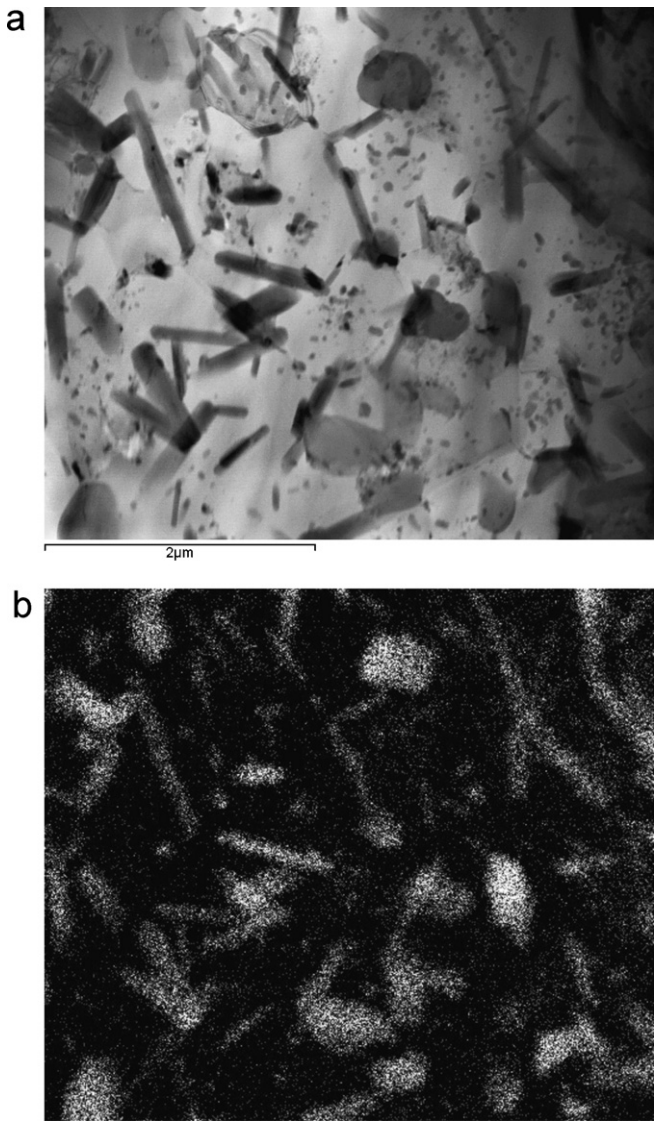

Fig. 8. Structure of the solution treated specimen (773 K for 30 min) deformed by compression at 773 K (ε_t = 0.39): (a) STEM image and (b) Mn-mapping results.

No quasicrystalline structures were reported. On the other hand, the addition of beryllium to the 93.5Al–5Mn–1.5Be (in wt.%) alloy improves the quasicrystal forming ability so effectively that the quasicrystalline structures are observed for the material manufactured by a conventional casting technique [43].

The very fine "C" particles, marked in Fig. 7a, were rich in Zn, Mg and Cu. Both the chemical composition of the Meso 20 alloy and the EDX analyses point to the development of an η-type phase [9–17]. Fine η-precipitates may grow during the air-cooling of the hot consolidated RS flakes (670 K).

A typical microstructure of a solution treated sample, deformed at 773 K, is presented in Figs. 8 and 9. The mapping of alloying elements confirmed the development of Mn-rich particles (Fig. 8b) and the uniform distribution of zinc (Zn-map is omitted).

Table 2
Average chemical composition of the Mn-rich rod-like particles in the solution treated sample deformed at 773 K.

	Al (at.%)	Mn (at.%)	Fe (at.%)	Cu (at.%)	Zn (at.%)
Average	81.3	11.6	0.2	4.5	2.5
Standard deviation	1.5	1.5	0.1	0.5	0.5

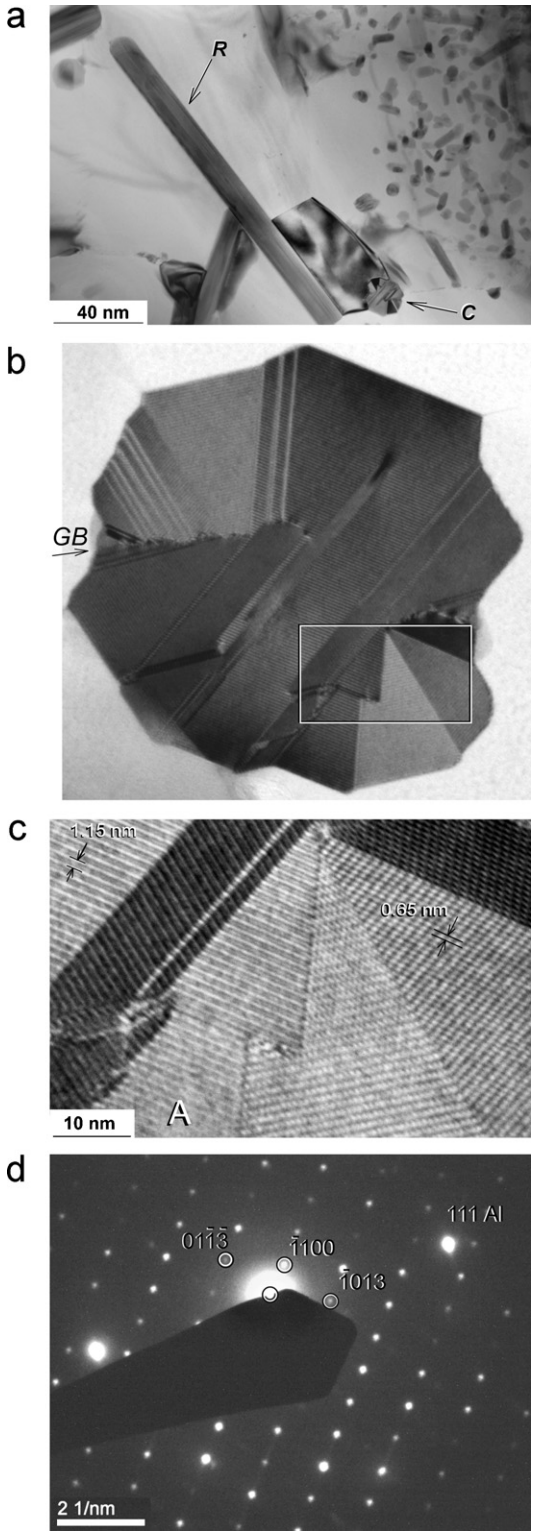

Fig. 9. Structure of the solution treated specimen (773 K for 30 min) deformed by compression at 773 K (ε_t = 0.39): (a) rod-like particle 'R' and the cross-sectioned rod-like Mn-rich particle 'C' marked in TEM image; (b) enlarged 'C' particle; (c) high resolution TEM image taken from the area marked in figure (b) and (d) SAD pattern received from the grain marked 'A' in figure (c).

Solution treatment and following deformation at 773 K was found to result in a dissolution of Zn-rich particles and transformation of Mn-rich metastable particles (quasicrystals) into the rod-like particles with length ranging 0.5–1 μm. The growth of the rod-like particle is accompanied by dissolution of the initial

Table 3
Structure of the intermetallic phases of the Al_xMn_y type, reported for the Al–Mn and 7000 series aluminum alloys.

Phase	Mn atomic %	Crystal structure, space group, or symmetry	References
$Al_{12}Mn$ (*G* phase)	0.077	Body-centered cubic, *Im3* $a = 0.747$ nm	[57] cited in [23] and [58] cited in [30]
		bcc, $Al_{12}W$-type $a = 0.7507$ nm	[22,47]
$Al_{78}Mn_{12}$	0.12	Quasi-crystalline structure, or oC1233, *Cmcm* $a = 2.41$ nm $b = 3.22$ nm $c = 2.40$ nm	[22,50]
$Al_{86}Mn_{14}$	0.14	Quasi-crystalline structure	[22,50]
Al_6Mn (I)	0.14	Quasicrystalline structure, which transform to stable orthorombic Al_6Mn during annealing at 673–773 K	[18,25]
Al_6Mn	0.14	Orthorhombic, *Cmcm* $a = 0.755$ nm $b = 0.649$ nm $c = 0.887$ nm	[24,25,27,30]
Al_4Mn (μ)	0.20	Hexagonal, $P6_3/m$ or $P6_3$ $a = 2.839$–2.841 nm $c = 1.240$–1.238 nm	[30,50]
		Hexagonal $a = 1.2295$ nm $c = 2.4634$ nm	[43]
		Hexagonal $P6_3/mmc$ $a = 1.995$ nm $c = 2.452$ nm	[23,49]
$Al_{4.12}Mn$ (μ) or Al_4Mn		Hexagonal, hP574, $P6_3/mmc$ $a = 1.998$ nm $c = 2.467$ nm	[23,48–53]
Al_4Mn (λ)		Hexagonal $P6_3/m$ $a = 2.838$ nm $c = 1.239$ nm	[23,30,48,50,53]
π-Al_4Mn		oC152, Cmcm $a = 0.77$ nm $b = 2.36$ nm $c = 1.24$ nm	[50]
T or T″ – heavily faulted variant of Al_4Mn	0.2	T: $PI0_5/mmc$ $a_1 = 0.3912$ nm $a_5 = 1.240$ nm	[22,50]
$Al_{10}Mn_3$ (φ)	0.23	Hexagonal, hP26, $P6_3/mmc$ $a = 0.754$ nm $c = 0.790$ nm	[23,50,53,54]
		bcc, $Al_{12}W$-type $a = 0.754$ nm	[59] cited in [55]
Al_3Mn or $Al_{11}Mn_4$ (HT)	0.25	Orthorhombic, *Pnma* $a = 1.259$ nm $b = 1.48$ nm $c = 1.242$ nm	[23,30,50]
$Al_{11}Mn_4$ (δ or I)*	0.27	Triclinic, $P\bar{1}$ $a = 0.5095$ nm $b = 0.8879$ nm $c = 0.5051$ nm $\alpha = 89.35^\circ$ $\beta = 100.47^\circ$ $\gamma = 105.08^\circ$	[23,24,28]
Al_8Mn_5 (γ_2)	0.38	Rhombohedral, Cr_5Al_8-type $a = 0.7756$ nm $\alpha = 109.03^\circ$	[60] cited in [55]
		Rhombohedral, *R*3 *m* $a = b = c = 0.906$ nm $\alpha = \beta = \gamma = 89.3^\circ$	[30]
		Hexagonal, *hR*3 $a = 0.4332$ nm $c = 0.2653$ nm or rhombohedral hRI $a = 0.2653$ $\alpha = 109.47^\circ$	[56]
AlMn (γ) (HT)[a] Above 1113 K		Cubic, W-type $a = b = c = 0.3062$ nm	[23,56]

* Metastable phase, which develops in the composition region for the stable μ-Al_4Mn. A metastable decagonal (D) phase is formed at a very high cooling rate and is observed along with the icosahedral (I) phase (18–22.5%Mn). The period of the *D* phase in the direction of the ten-fold axis is equal to ~1.2 nm.

[a] High-temperature phase cannot be retained by quenching.

fine grained Mn-rich particles in the neighboring matrix. The average chemical content of the particles was measured by EDX and is presented in Table 2. The chemical composition of the particles indicates possible atomic stoichiometry of Al:Mn = 8:1 or Al:(Mn,Fe,Cu,Zn) = 4.3:1. However, the aluminum content in the Al:Mn ratio can be higher than the stoichiometry of the tested phase because of the known effect of an extra excitation of the Al-atoms in the matrix surrounding fine particles. If it is assumed that Fe, Cu and Zn atoms are substituting some Mn atoms, the average atomic stoichiometry becomes close to 4:1, which may suggest the Al_4Mn structure development.

Further high resolution TEM observations were carried out to investigate the structure and crystallography of Mn-rich rod-like precipitates. An example of two precipitates in shown in Fig. 9a. It may be seen that when the Mn-rich rod-like particle (R) is aligned longitudinally on the thin foil it exhibits striated structure. On the other hand, on a plane perpendicular to the particle axis, the particle is of a polyhedron shape and has fairly complex internal structure, as shown in Fig. 9a (marked by C) and Fig. 9b. This complex structure consists of multi-twins rotated by 35.6° for each twinning step; details are presented in Fig. 9c. The multiplication of twinning angles does not sum to 360° and therefore a high angle grain boundary (GB) must form between the rod center and the external layer of the rod. It has to be noted that similar structures of the Al_xMn_y phases were not reported in the literature yet, and commonly observed Mn-rich particles in industrial materials exhibit different structures and morphology. In order to analyze its crystallographic structure the crystallographic data for several Al_xMn_y phases reported in the literature were collected. These are summarized in Table 3. Couple interplanar distances are measured on the image presented in Fig. 9c, and the SAD pattern taken from the area indicated by letter A is presented in Fig. 9d. No fit was found for the Al_6Mn or $Al_{12}Mn$ structures listed in Table 2. The best fit of the currently investigated particle was found for the μ-Al_4Mn hexagonal phase, $a = 2.841$ nm, $c = 1.238$ nm [43]. Both interplanar distances d_{hkil} calculated from diffraction spots and measured directly from the HREM picture were very close to those calculated for the μ-Al_4Mn.

It may be noted in the SAD pattern (Fig. 9d) that the angle 35.6 deg between the diffraction spots corresponds to the angle between $(0\,1\,\bar{1}\,\bar{3})$ and $(\bar{1}\,0\,1\,3)$ twinning planes in the hexagonal μ-Al_4Mn structure. The last statement leads to the conclusion that the particle has grown along the $[3\,\bar{3}\,0\,1]$ zone axis.

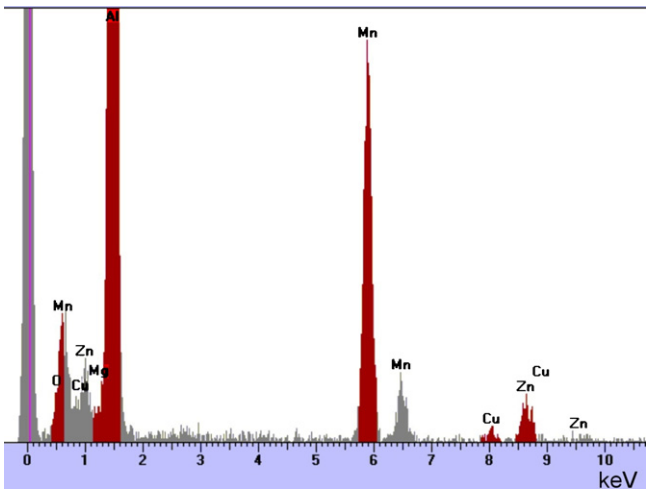

Fig. A1. Typical EDX spectrum received from the particles observed in RS flake (The spectrum was received from the particle marked with an arrow in Fig. 5).

4. Conclusions

1. Rapid solidification of Meso 20 alloy results in the growth of fine Al(Mn, Cu, Zn) particles of the average length of 11.5 nm and thickness of 8.6 nm. TEM observations revealed complex non-Bravais structure of particles, which is typical for the metastable quasicrystalline Mn-rich phase. Thin Zn-rich layer on the pre-existing Mn-rich particles was ascribed to the heterogeneous nucleation of the η-type precipitates.

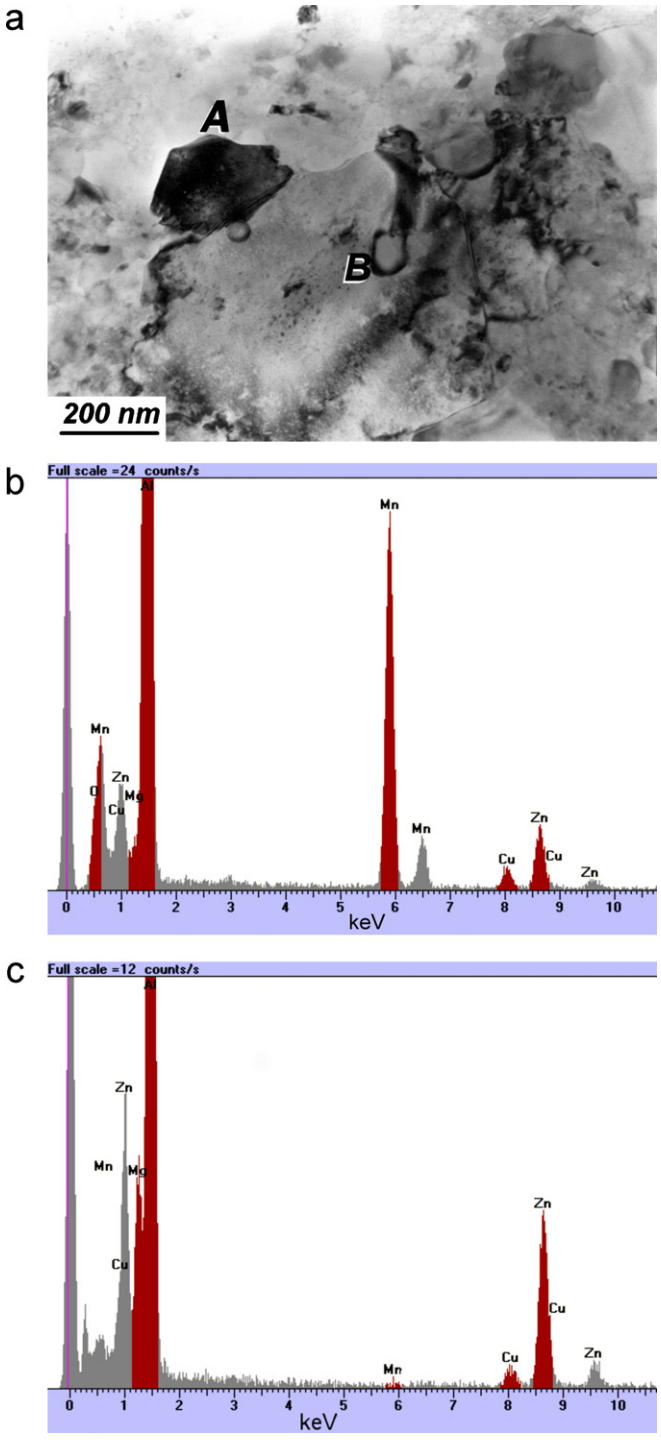

Fig. A2. Structure of the as-extruded rod: (a) TEM image; (b) EDX spectrum received from the particle marked "A" in TEM image and (c) EDX spectrum received from the particle marked "B".

2. As-extruded Meso 20 RS alloy is characterized by relatively high flow stress level at the high temperature deformation. The material does not fracture at deformation temperature 443–773 K within the true strain range applied in the compression tests, i.e. $\varepsilon_t \leq 0.4$.
3. The structure of the as-extruded Meso 20 RS alloy is characterized by the development of irregular *T*-phase particles (50–150 nm in size) and very fine Mn-rich quasicrystalline particle development. The growth of both *T*-phase and some fine η-type particles can mostly result from the RS flakes' consolidation procedures i.e. the hot compression of the RS flakes and the vacuum degassing at 670 K.
4. Solution treatment at 773 K for 30 min of the extruded material results in the flow stress reduction. The dynamic precipitation hardening effect was practically negligible which is in contrary to other hardenable aluminum alloys. Relatively low dynamic precipitation hardening in the ST Meso 20 alloy possibly can be attributed to the privileged heterogeneous precipitation of the η-type phase on the interfacial boundaries of the fine Mn-rich particles and other structural defects.
5. Solution treatment at 773 K for 30 min results in precipitation of rod-like μ-Al_4Mn particles unique to this processing method. Precipitates are twinned along the long axis as manifested by striated contrast in the TEM. The radial distribution of some twinning-type planes was found to form a star-like structure observed on the perpendicular cross-section of the particle.

Acknowledgments

The authors are very grateful to Professor Junichi Kaneko for his remarkable contribution to the research project and the valuable discussion of the results. The authors are grateful to Professor Wlodzimierz Bochniak for his assistance during KOBO extrusion and Dr. Tomasz Tokarski for the LatticeCalc program development and his help with the crystallography analysis. The financial support within the Grant No. 507 100 32/2955 is kindly acknowledged.

Appendix A.

See Figs. A1 and A2.

References

[1] K. Seimiya, M. Sugamata, L. Blaz, J. Kaneko, J. Jpn. Soc. Powder Powder Metal. 53 (2006) 899–9083.
[2] J. Kaneko, M. Sugamata, L. Blaz, R. Kamei, Mater. Sci. Forum 396–402 (2002) 161–166.
[3] L. Blaz, M. Sugamata, J. Kaneko, J. Sobota, G. Wloch, W. Bochniak, A. Kula, J. Mater. Process. Technol. 209 (2009) 4329–4336.
[4] M. De Sanctis, Mater. Sci. Eng. A141 (1991) 103–121.
[5] G.E. Totten, D.S. Scott MacKenzie (Eds.), Handbook of Aluminum, vol. 1, Physical Metallurgy, Processes, Marcel Dekker Inc., New York, Basel, 2003.
[6] K. Raju, S.N. Ojha, A.P. Harsha, J. Mater. Sci. 43 (2008) 2509–2521.
[7] E. Salamci, R.F. Cochrane, Mater. Sci. Technol. 18 (2002) 1445–1452.
[8] E. Salamci, R.F. Cochrane, Mater. Sci. Technol. 19 (2003) 1130–1136.
[9] E. Salamci, Mater. Sci. Technol. 20 (2004) 859–863.
[10] J.D. Robson, Mater. Sci. Eng. A A382 (2004) 112–121.
[11] D. Godard, P. Archambault, E. Aeby-Gautier, G. Lapasset, Acta Mater. 50 (2002) 2319–2329.
[12] R. Ferragut, A. Somoza, A. Tottley, A. Torriani, J. Mater. Process. Technol. 141 (2003) 35–40.
[13] J. Gjonnes, C.H.R.J. Simensen, Acta Metall. 18 (1970) 881–890.
[14] S.P. Ringer, K. Hono, Mater. Charact. 44 (2000) 101–131.
[15] A.K. Mukhopadhyay, Philos. Mag. Lett. 70 (1994) 135–140.
[16] L.F. Mondolfo, N.A. Gjostein, D.W. Levinson, Trans. AIME (1956) 1378–1385.
[17] L.K. Berg, J. Gjonnes, V. Hansen, X.Z. Li, M. Knutson-Wedel, G. Waterloo, D. Schryvers, L.R. Wallenberg, Acta Mater. 49 (2001) 3443–3451.
[18] D. Shetchman, I. Blach, D. Gratias, J.W. Cahn, Phys. Rev. Lett. 53 (1984) 1951–1954.
[19] T. Fujiwara, T. Ogawa (Eds.), Quasicrystals, Solid-State Science, vol. 93, Springer-Verlag, Heidelberg, 1990.
[20] M. Senechal, Quasicrystals and Geometry, Cambridge Univ. Press, 1995.
[21] R. Divakar, D. Sundararaman, V.S. Raghunathan, Prog. Cryst. Growth Charact. 34 (1997) 263–269.
[22] T. Rajasekharan, J.A. Sekhar, Scripta Metal. 20 (1986) 235–238.
[23] B. Grushko, T.Ya. Velikanova, Powder Metall. Met. Ceram. 43 (2004) 72–86.
[24] A. Kontio, P. Coppens, Acta Crystallogr. B37 (1981) 433–435.
[25] K. Saksl, D. Vojtech, H. Franz, J. Mater. Sci. 42 (2007) 7198–7201.
[26] S. Ruan, C.A. Schuh, Acta Mater. 57 (2009) 3810–3822.
[27] N.A. Bielov, D.G. Eskin, A.A. Aksenov (Eds.), Multicomponent Phase Diagrams, Applications for Commercial Aluminum Alloys, Elsevier Ltd., Oxford, 2005.
[28] A. Kontio, E.D. Stevens, P. Coppens, Acta Crystallogr. B36 (1980) 435–436.
[29] R.A. Dunlap, K. Dini, Can. J. Phys. 63 (1985) 1267.
[30] J. Chang, I. Moon, Ch. Choi, Metal. Mater. Trans. 29A (1998) 1873–1882.
[31] W. Bochniak, A. Korbel, Mater. Sci. Technol. 16 (2000) 664–669.
[32] W. Bochniak, A. Korbel, J. Mater. Process. Technol. 134 (2003) 120–134.
[33] W. Bochniak, A. Korbel, Mater. Sci. Forum 331–333 (Part 1–3) (2000) 613–617.
[34] K.U. Kainer, Metal Matrix Composites, WILEY-VCH Verlag GmbH & Co, KgaA, 2006.
[35] T. Laha, A. Agarwal, T. McKechnie, K. Rea, S. Seal, Acta Mater. 53 (2005) 5429–5438.
[36] J.M. Papazian, Metal. Trans. 13A (1982) 761–769.
[37] C.-Y. Shieu, S.-J. Lin, J. Mater. Sci. 32 (1997) 1741–1747.
[38] A. Kula, L. Blaz, J. Koziel, M. Sugamata, G. Wloch, Problems of Modern Techniques in Engineering and Education – 2008, Pedagogical University of Cracow, 2008, pp. 63–68.
[39] L. Blaz, E. Evangelista, Mater. Sci. Eng. A207 (1996) 195–201.
[40] L. Blaz, A. Korbel, W. Bochniak, Z. Rdzawski, in: Y. Hosoi, et al. (Eds.), Proc. 7th JIM Intern. Symp. (JIMIS7), The Japan Institute of Metals, Nagoya, Japan, 1993, pp. 287–294.
[41] I. Weiss, J.J. Jonas, Metal. Trans. 10A (1979) 831–840.
[42] L. Blaz, E. Evangelista, M. Niewczas, Metal. Mater. Trans. 25A (1994) 257–266.
[43] H.J. Chang, E. Fleury, G.S. Somg, W.T. Kim, D.H. Kim, J. Non-Cryst. Solids 334 and 335 (2004) 12–16.
[44] L. Blaz, K. Piela, Key Eng. Mater. 188 (2000) 83–90.
[45] L. Blaz, K. Piela, Mater. Sci. Technol. 23 (2007) 1–7.
[46] J. Koziel, L. Blaz, A. Kula, M. Sugamata, G. Wloch, in: V. Hrnčiar (Ed.), Proc. 11-th Intern Conf., Technology 2009, Bratislava 2009 Sept. 9–10, 2009, pp. 88–91.
[47] J. Adam, J.B. Rich, Acta Crystallogr. 7 (1954) 813–816.
[48] M. Uchida, Y. Matsui, Philos. Mag. A81 (2001) 2121–2126.
[49] C.B. Shoemaker, D.A. Keszler, D.P. Shoemaker, Acta Crystallogr. B45 (1989) 13–20.
[50] G. Kreiner, H.F. Franzen, J. Alloys Compd. 261 (1997) 83–104.
[51] M. Uchida, S. Horiuchi, J. Appl. Crystallogr. 32 (1999) 417–420.
[52] D. Nguyen-Manh, G. Trambly de Laissardiere, J. Magn. Magn. Mater. 262 (2003) 496–501.
[53] G. Kreiner, H.F. Franzen, J. Alloys Compd. 221 (1995) 15–36.
[54] M.A. Taylor, Acta Crystallogr. 12 (1959) 393–396.
[55] Landolt-Bornstein, in: W. Martienssen (Ed.), Numerical Data and Functional Relationships in Science and Technology, New Series, Springer-Verlag, Berlin/Heidelberg/New York, 1998.
[56] M. Ellner, Metal. Trans. 21A (1990) 1669–1672.
[57] P. Villars, L.D. Calvert, Pearson's Handbook of Crystallographic Data for Intermetallic Phases, ASM, Metal Park, Ohio, 1991.
[58] G. Marchand, J. Inst. Met. 73 (1946) 747–749.
[59] D.B. Goel, U.P. Roorkee, P. Furrer, H. Warlimont, Aluminum 50 (1974) 511.
[60] H.G. Meissner, K.Z. Schubert:, Metallkde 56 (1965) 523.